

Fully Digital Beamforming Receiver With a Real-Time Calibration for 5G Mobile Communication

Dong-Chan Kim^{ID}, Seong-Jin Park^{ID}, Tae-Wan Kim^{ID}, Laxmikant Minz,
and Seong-Ook Park^{ID}, *Senior Member, IEEE*

Abstract—This paper presents a fully digital beamforming receiver (FDBR) using a method that calibrates the signals of all chains in real time, and is targeted for 5G mobile communication. In the real-time calibration method, the received signals of all chains are adjusted to correct the errors of phase and amplitude using the in-band signal other than operating frequency for calibration. The proposed FDBR with real-time calibration is designed and fabricated. The FDBR consists of eight chains of the tapered slot antenna (TSA) element, low noise block (LNB), and software defined radios (SDRs). The 1×8 array TSA with the directional coupler and the 1:8 divider is designed to send eight uniform calibration signals along with the received signal of all the chains. In SDR, the digital phase shifter and the real-time calibration blocks are implemented to realize digital beamforming. The digital phase shifter has an extremely high resolution of 0.72° . After using the real-time calibration method, the average of measured phase and amplitude error between each chain is less than 0.9° and 0.5 dB, respectively. To verify the beamforming performance of the FDBR, the simulation radiation pattern and the measurement radiation pattern are compared for 0° , $\pm 15^\circ$, $\pm 30^\circ$, and $\pm 45^\circ$ beam angles. The simulation results are in good agreement with the measured results. An excellent beamforming performance is achieved in the 1×8 array FDBR using the real-time calibration.

Index Terms—Antenna arrays, beam steering, calibration, digital signal processors, millimeter-wave (mm-wave) receivers.

I. INTRODUCTION

RECENTLY, there has been a growing interest in beamforming techniques for fifth-generation (5G) communication [1]–[3]. Beamforming is one of the key techniques

Manuscript received July 16, 2018; revised January 25, 2019; accepted February 16, 2019. Date of publication March 4, 2019; date of current version May 31, 2019. This work was supported in part by the Institute for Information and Communications Technology Promotion Grant funded by the Korea government (MSIP) through Study on Measurement and Evaluation Technology based on Reverberation Chamber under Grant 2015-0-00855 and in part by the Institute for Information and Communications Technology Promotion Grant funded by the Korea government (MSIT) through Development of testing and verification technology for 5G mobile communications supporting enhanced mobile broadband (eMBB), ultra reliable/low latency communication (URLLC), and machine-type communications (mMTC) under Grant 2018-0-00733. (*Corresponding author: Dong-Chan Kim.*)

D.-C. Kim, T.-W. Kim, L. Minz, and S.-O. Park are with the Microwave and Antenna Laboratory, School of Electrical Engineering, Korea Advanced Institute of Science and Technology, Daejeon 34141, South Korea (e-mail: kdch5204@kaist.ac.kr; gold427@kaist.ac.kr; lkminz@kaist.ac.kr; soparky@kaist.ac.kr).

S.-J. Park is with Samsung Electronics Co., Ltd., Suwon 443-743, South Korea (e-mail: pondsky@kaist.ac.kr).

Color versions of one or more of the figures in this paper are available online at <http://ieeexplore.ieee.org>.

Digital Object Identifier 10.1109/TAP.2019.2902712

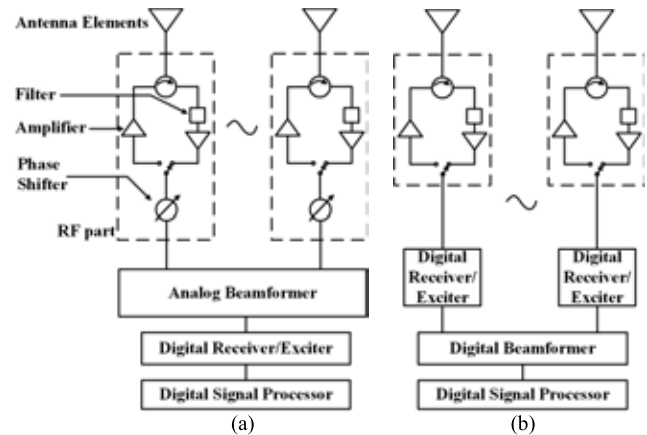


Fig. 1. (a) Active beamforming architecture. (b) Fully digital beamforming architecture.

used to overcome high path loss at the millimeter-wave (mm-wave) band and to distinguish multiple users. Due to the great potential beamforming has, various beamforming architectures such as active beamforming structure, hybrid beamforming structure, and fully digital beamforming structure have been proposed and studied [4], [5].

The block diagram of an active beamforming architecture is shown in Fig. 1(a). In the active beamforming architecture, the amplifiers and the phase shifters are distributed to each radio frequency (RF) chain, and the analog combiner is located after the phase shifters.

This architecture has the advantage of overcoming the RF loss between the amplifier and free space and reducing the noise figure. However, the RF parts in this architecture are complex, high in cost, and vulnerable to heat and power consumption. In addition, the beamforming performance of this architecture is not guaranteed due to usages of a chip-based phase shifter, which does not provide high-resolution control and linear characteristic [6]–[8]. The low-resolution and nonlinear characteristics of the phase shifter cause discrete beamforming performance and reduction in the gain of the main beam.

In a fully digital beamforming architecture, as shown in Fig. 1(b), the phase shifters in the RF parts are replaced by digital phase shifters in the digital signal processor part, and the analog beamformer is replaced by the digital beamformer. This architecture eliminates the disadvantage of active

beamforming and the digitized signals of all chains offer a high degree of freedom in signal processing. These advantages in signal processing enable us to perform a variety of signal processing such as ultralow sidelobe, improved adaptive pattern nulling and multiple simultaneous beams, which are found to be difficult to perform through other architectures [5]. However, to realize the digital beamforming technique, there are several challenges related to hardware implementation. In order to obtain stable performance, the phase and amplitude of signals in all chains should be identical between each chain. The RF active components in a system such as amplifier and mixer are greatly affected by the temperature variation and fabrication error [9]–[11]. Such influence on active components causes the phase and the amplitude errors between each chain. The discrepancy directly leads to inaccurate beam direction and large sidelobe level [18].

Several approaches have been proposed to reduce these errors [10]–[14]. In [10], the calibration method can only correct phase and amplitude errors of the signal after the mixer, excluding the LNA and bandpass filter (BPF) of the receiver. In the 5G mobile communication band, the error generated in the LNA and PA of the RF front end is critical to the system. Therefore, the method used in [10] is not sufficient to use in 5G mobile communication. In [11], additional chips such as a phase shifter, a switch, and a chip for measuring the phase and amplitude error are added for beamforming and calibration. As a result, the system cost increased and due to many additional components needed for calibration, the heating effect worsened the beamforming performance [15]. For these reasons, the beamforming structure and calibration method in [11] is not suitable for 5G mobile communication. In the case of mutual coupling-based calibration method in [12] and [13], accurate measurement of the mutual coupling will be difficult because the array antenna is not arranged regularly and there are various parts around the antenna in the smartphone [16], [17]. In the SAR system [14], the signal change by the internal active component is measured using the Tx signal and Rx signal and saved as table. Then, the table is used to compensate for error when signal processing on the ground. The method does not consider real-time calibration. The calibration methods in [10]–[14] are suitable for individual purpose, but they are not sufficient to use in 5G mobile communications.

Therefore, a new type of calibration for the phase and amplitude errors in real time is essential for 5G communication. Real-time calibration methods using a calibration signal at below 6 GHz have been proposed [19], [20]. In [19] and [20], a calibration signal is simply applied using a coupler. Because the critical errors of phase and amplitude are generated in the active component at the RF front end, the calibration signals with uniform phase and amplitude should be applied after the antenna and be used at mm-wave band in order to calibrate every active component in the receiver. Compared to below 6 GHz, the signal loss at mm-wave band would be very high and the phase error would have a critical effect on the signal. In addition, since the spacing between the antennas is very narrow at the mm-wave band, there are considerable difficulties in applying the calibration signal.

Therefore, the system structure in [19] and [20] is not sufficient to use in the 5G mobile communication band.

In this paper, the validity of applying the real-time calibration method in the implementation of the digital beamforming at the 5G mobile communication band is verified and the fully digital beamforming receiver (FDBR) that can simultaneously perform beamforming and the real-time calibration for 5G mobile communication and solve the difficulties in applying the calibration at mm-wave band is proposed.

The calibration method is composed of two parts. The main purpose of each part is the elimination of offset error and variation error. Each offset error is eliminated by measuring the difference of the phase and amplitude between the signals in the eight chains. Second, a variation error can be removed using the principle that the phase and amplitude variation of active components in system in-band signals have similar tendency depending on temperature. An in-band signal other than operating frequency is introduced as a calibration signal to remove the variation error in real time. A 1×8 array tapered slot antenna (TSA) with directional coupler and a 1:8 divider is designed to apply the calibration method in the FDBR. Along with that, a new type of digital phase shifter and calibration block is also implemented in signal processing part to apply the calibration method to the FDBR. Unlike previous research on calibration, the proposed FDBR structure is inexpensive because it does not use additional chips for calibration and beamforming and uses a low-cost coupler and divider, considering the proper method for applying the calibration signal at mm-wave band. After calibration, the average errors of the phase and amplitude between each chain are significantly reduced. In order to support the validity of the FDBR with the real-time calibration method, the radiation pattern was measured in an anechoic chamber (AC) at 28 GHz, and the results are in a good agreement.

This paper is organized as follows. Section II discusses the architecture of the FDBR with the real-time calibration. Section III describes the 1×8 array TSA in the FDBR. In Section IV, the signal processing part in the software defined radio (SDR) is explained. The performance of the real-time calibration and the proposed FDBR with the calibration is verified in Section V. Finally, the conclusion is given in Section VI.

II. ARCHITECTURE OF THE FDBR AND REAL-TIME CALIBRATION

A. Architecture and Errors of the FDBR

The architecture of the proposed FDBR with real-time calibration is presented in Fig. 2. The FDBR consists of eight chains of TSA elements, low noise block (LNB), and SDR. All the chains are connected to the signal processing part. The 1×8 array of TSA and the signal processing part are discussed in detail later.

In the FDBR, LNBS amplify the received signal and convert the RF signal to the IF signal with minimal noise and are shielded with a metal case to prevent interference between each chain. The LNB is composed of filters, an amplifier, a mixer, and a two times doubler. The measured specification of the LNB is listed in Table I.

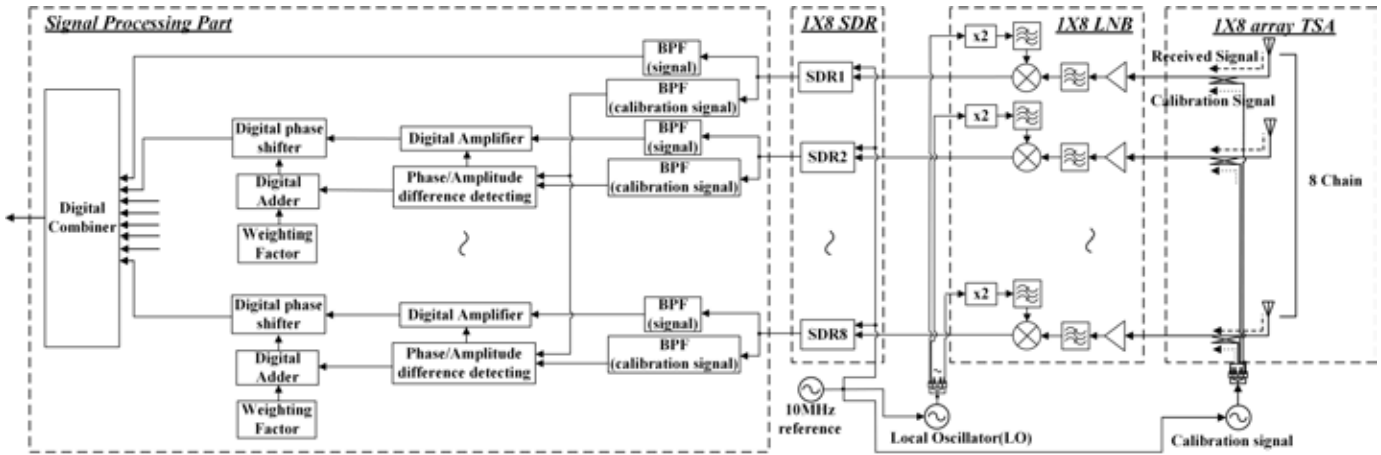


Fig. 2. Architecture of the FDBR.

TABLE I
SPECIFICATION OF THE LNB

THE SPECIFICATION	
RADIO FREQUENCY (GHz)	27.00885 ~ 29.0085
LOCAL OSCILLATOR FREQUENCY (GHz)	14.30225 ~ 15.30225
DYNAMIC RANGE (dB)	120
CONVERSION GAIN (dB)	17
FLATNESS (dB)	< 1

TABLE II
SPECIFICATION OF THE SDR

THE SPECIFICATION	
RECEIVED FREQUENCY (GHz)	0.001 ~ 6
GAIN OF VGA IN IF (dB)	0 ~ 40
GAIN OF VGA IN BASE BAND(dB)	0 ~ 62
SAMPLING RATE (MHz)	< 20
FLATNESS (dB)	< 1
MAXIMUM DYNAMIC RANGE (dB)	75

TABLE III
MEASURED ERRORS (UNIT: DECIBEL AND DEGREE)

		Without Calibration							
		Chain							
	Errors Type	1	2	3	4	5	6	7	8
Amplitude	Offset	0	-1.9	2.1	-1.4	3.2	4.9	0.5	1.7
	Variation Range	0	1.8	0.4	1.2	1.7	1.5	0.8	1.0
Phase	Offset	0	29	79	1	85	-10	-11	-49
	Variation Range	0	43	20	42	32	65	52	38

Another unit in FDBR is the SDR. SDR is a radio communication system to receive and transmit signal. The SDR consists of variable gain amplifiers (VGAs), an analog-to-digital converter (ADC), and an IQ demodulator. The measured specification of the SDR is listed in Table II. The IQ signals in the SDR are transferred to the computer, and processed through a signal processing program (GNUradio). GNUradio processes the signal in block units which can be easily implemented and can be directly coded, if necessary.

The performance issue of the FDBR architecture can be evaluated by measuring the signals in eight chains of the FDBR for any phase and amplitude difference. We measured the signals in eight chains for 4 h without the calibration. The measurement is performed in far-field AC at 28 GHz. All chains are compared in terms of the phase and amplitude with respect to chain 1. The measured errors of the eight chains are listed in Table III. Fig. 3(a) and (b) presents the phase and amplitude variation in chains 2–4 relative to chain 1 for 4 h.

There are offset errors and time-dependent variation errors in 4 h measurement. In addition, the tendencies of the phase

and amplitude variation differ from chain to chain. The maximum amplitude offset among eight chains is 4.9 dB and the maximum variation range of amplitude in the eight chains after removing the amplitude offsets is 1.8 dB. The maximum phase offset among the eight chains is 85° and the maximum variation range of phase in the eight chains after elimination of the phase offset is 65°. The phase errors are relatively large compared to the amplitude errors in all chains. To identify the impact of the errors on the performance of beamforming, the pattern of the array factor with/without errors are computed on the basis of the measurement result of phase and amplitude error and plotted in Fig. 3(c). Comparing the pattern of array factor with error after 4 h to that without error, the main beam direction is tilted up to 40° and the sidelobe level is increased up to 8.5 dB. Thus, it is apparent that such errors could hinder the system to distinguish multiple users and increase the interference.

There are two main causes of phase and amplitude errors. The first is a time-independent error, which is due to a physical and manufacturing error that occurs in wire bonding and soldering. This error is inevitable and creates different offset of phases and amplitudes in each chain. Such an error is not dependent on time, and therefore, can be easily removed from the signal in each chain by measuring and eliminating the offset once. The second is a time-dependent error. As the property of active components can be altered by a change in the system temperature, a gradual generation of heat by the

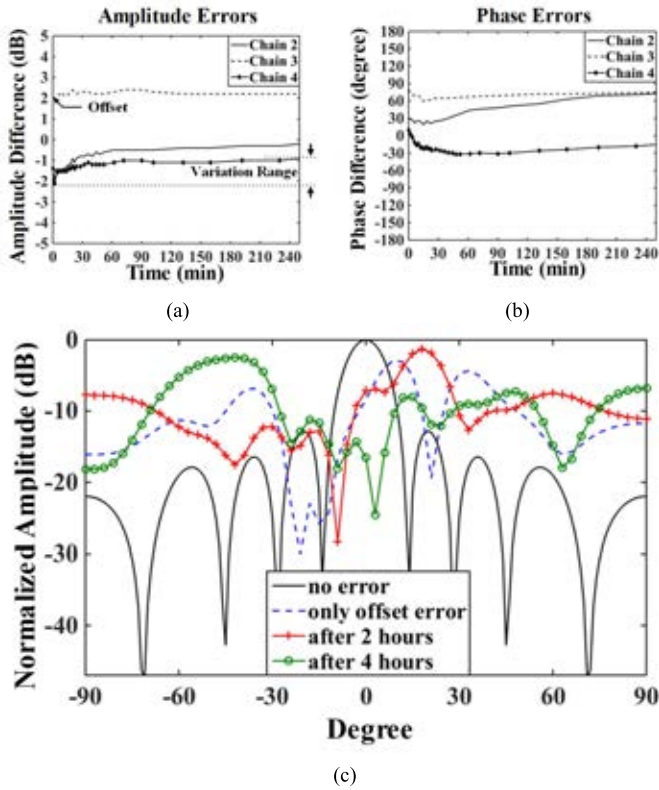


Fig. 3. Errors in the FDBR for 4 h. (a) Amplitude. (b) Phase. (c) Pattern of the array factor with/without errors.

system components or a sudden change of environment can result in a time-dependent error. Even for the same products, the effect of the temperature and the tendency of error variation can differ depending on the fabrication condition. The variation of active component property due to the temperature is directly related to the variation of the threshold voltage and carrier mobility with the temperature [9]. Examining the measurement or simulation results in [9] and [21]–[24], it can be observed that the phase and amplitude of signals with frequencies within bandwidth of active components change with the similar tendency depending on the temperature. Therefore, using a calibration signal of frequency within bandwidth of the system but different to the frequency of the received signal, the phase and amplitude variation of the received signal due to the temperature can be detected by measuring the phase and amplitude variation of the calibration signal.

To verify this property, we measured the phase and amplitude variation by injecting the received signal and the calibration signal into all chains of the FDBR at the same time. The received signal is at 28 GHz and the calibration signal is at 28.002 GHz. The received signal and the calibration signal produce the amplitude variation and the phase variation with different offsets as they are of different wavelengths. However, the tendency of variation in both signals would be similar. The amplitude and the phase variation of received signal and calibration signal in chains 2–4 with respect to chain 1 after attuning the offset is shown in Fig. 4. The amplitude variation of the two signals in all chains has the same tendency and

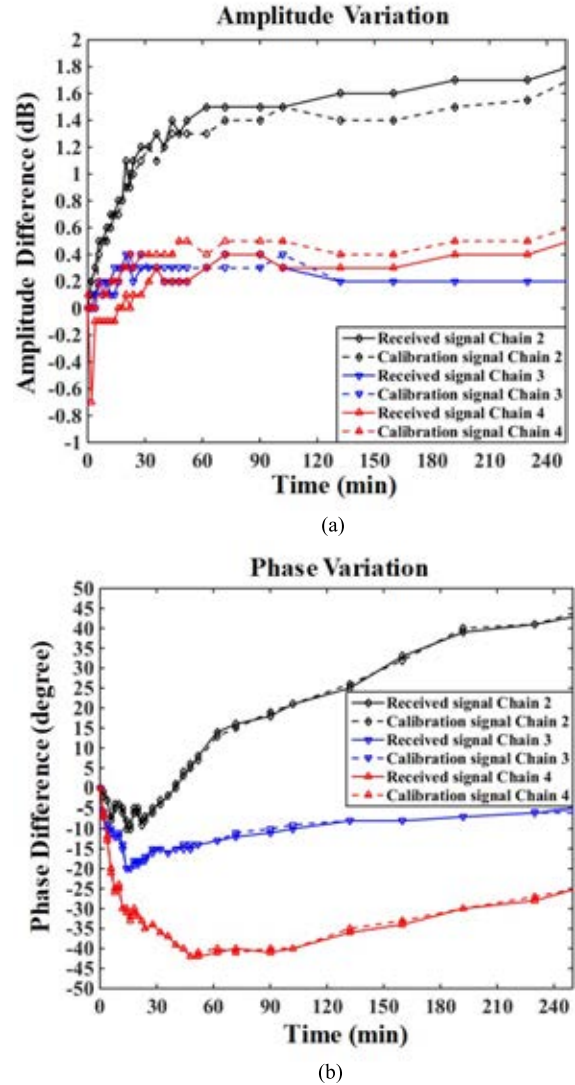


Fig. 4. Measured result of the signal between different frequencies. (a) Amplitude. (b) Phase.

the maximum difference between two signals is 0.2 dB. Also, the phase variation of the two signals has the same tendency and the maximum difference between two signals is 0.7° . It is demonstrated that two signals with different frequencies in the system bandwidth have almost identical variation of the phase and amplitude. In the real-time calibration, using this characteristic of the active components, the calibration signal can be used to detect the phase and amplitude error of the received signals in all chains.

B. Real-Time Calibration in the FDBR

The real-time calibration is applied to calibrate the offset and amplitude/phase variation error in each chain. In the FDBR, the calibration signal is introduced to detect the phase and amplitude difference of the received signal between each chain in real time. Before that, the offset is removed individually for received signal and calibration signal because the frequency of the received signal is different from the frequency of the calibration signal. The offset of the received signal

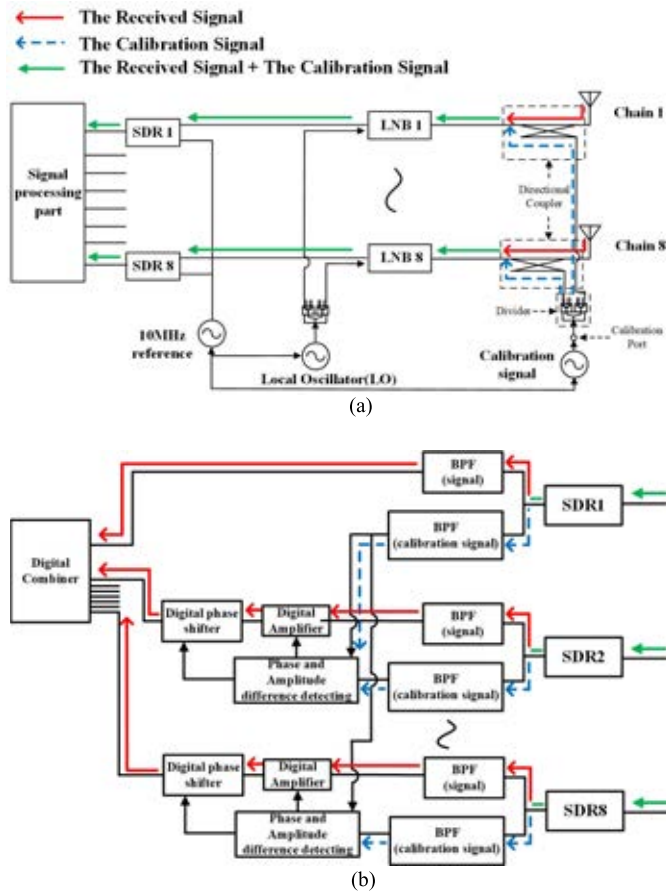


Fig. 5. Flow of the calibration signal and the received signal. (a) Hardware part. (b) Signal processing part.

is measured and removed first by measuring the signals in eight chains of the FDBR only for received signal without any calibration signal. Later, the offset of the calibration signal is measured and removed by injecting the calibration signal into the calibration port in the previous measurement setup. After elimination of the offset, the calibration signal injected into the calibration port is divided into eight identical calibration signals as shown in Fig. 5(a). Each calibration signal is combined with the received signal through directional coupler, and then, the combined signals pass through the LNA and the SDR. The combined signal is separated at the signal processing part using the BPF, and then, the phase and amplitude of the received signals in each chain are calibrated in real time through signal processing using the separated calibration signals as shown in Fig. 5(b). This calibration method is susceptible to interference problems because the received signal and the calibration signal pass through the system together. In the proposed FDBR, the interference is sharply removed by using a digital BPF that has minimum bandwidth of 1 kHz.

The real-time calibration process, as in the following steps, is very simple and corrects the offset errors and the variation errors.

The real-time calibration process.
 [Remove offset of received signal]

Step 1: Input the signal with the frequency in concord with the frequency of the received signal.

Step 2: Measure the offset of the amplitude and the phase at the frequency of the received signal in all chains, compared with chain 1.

Step 3: Remove the offset based on measured value.

[Remove offset of calibration signal]

Step 4: Input the calibration signal to calibration port.

Step 5: Measure the offset of the amplitude and the phase at the frequency of the calibration signal in all chains compared with chain 1.

Step 6: Remove the offset based on measured value.

[Remove variation error of received signal]

Step 7: The phase and amplitude variation of the calibration signals in all chains with respect to chain 1 is detected and, based on that, received signal variation errors of all the chains are automatically compensated.

Steps 1–3 have been carried out to remove the offset errors of the received signal. Steps 4–6 are needed to remove the offsets of the calibration signal. Finally, in step 7, the phase and amplitude variation error in chains are removed.

III. ANTENNA DESIGN

A. Antenna Configuration

The mm-wave 1×8 array antenna is designed to facilitate eight receivers and to apply the calibration signal to beamforming system at the 5G mobile communication band (28 GHz band). The antenna is composed of the TSA element, a multilayer substrate-integrated waveguide (SIW) directional slot coupler, and an eight-way SIW divider. In TSA array design, a TSA is a very compact antenna model and it is very convenient to arrange the antenna elements with half-wavelength distance from each other. In addition, it is easier to obtain a wide beam scanning sector in the horizontal direction from TSA array [26]. Based on the corrugated antipodal linearly TSA (CALTSA) design guideline published in [31], the single element is designed. An SIW structure is used to form coupler and divider because it has low loss at high frequency, low fabrication cost and it can be easily connected with other circuits. The SIW divider is designed to uniformly separate the signal into eight-way using the structure in [27]. The directional coupler is designed to combine the calibration signal with the received signal using a multilayer slot in [28]. The structures of the divider and coupler are easy to design and cheap to fabricate. The SMP-to-SIW transition is designed to solve the spatial problem, based on the transition in [29].

The proposed TSA array consists of a stack of two layers as shown in Fig. 6. The top layer of the proposed antenna contains an eight-element TSA array, SIW-based RF lines, and receiving ports. The bottom layer includes an eight-way power divider and eight-way power combiner. At the center of the proposed antenna, there are eight multilayer directional couplers to combine the calibration signal with the received signal. The received signal successively passes TSA elements, SIW-based RF lines, and receiving ports. The calibration signal is applied through the calibration port, and then, the signal successively passes the eight-way power divider, multilayer

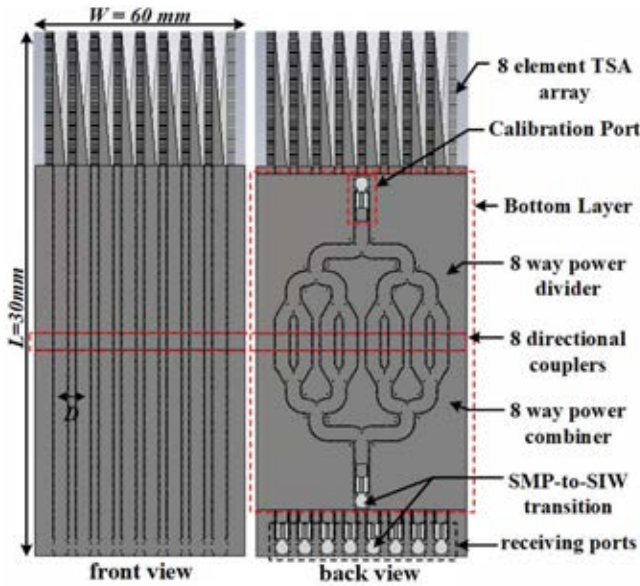


Fig. 6. Geometry of the proposed TSA array with calibration coupler.

directional coupler, SIW-based RF lines, and receiving ports. The eight-way power combiner on the backside is designed to check and verify the signal that combined the received signal and calibration signals through the directional couplers. As receiving ports, the SMP-to-SIW transition is used to extract the signal and input the signal to the LNB.

The distance (D) between two antenna elements is 5.65 mm, which is about the half-wavelength at 28 GHz. In the proposed design, the substrates are made of Rogers 4350B laminate with a thickness of 0.508 mm, dielectric constant of 3.66, and tangent loss of 0.004. The overall size is 60 mm (W) \times 150 mm (L). SIW parameters such as the width, the via diameter, and the gap between two vias are chosen to avoid any bandgap phenomenon within the operating frequency band and minimize the guided-wave transmission losses. In the proposed design, the SIW width, the via diameter, and the gap between two vias are chosen as 3.65, 0.4, and 0.6 mm, respectively. The SIW parameters can be determined by the formulas introduced in [30].

B. Eight-Way Power Divider and Double-Layer SIW Directional Coupler

The performance of the SIW-based divider and directional coupler is important for the calibration signal to induce properly in 28 GHz and is verified through the simulation results after design. Each output port in the eight-way power divider is individually simulated for checking the performance of the feeding network. Fig. 7 represents the geometry and the simulation result of the amplitude and the phase of the eight-way power divider. The reflection coefficient ($|S_{11}|$) of the divider is less than -20 dB over the operating frequency band. In addition, the output amplitude and phase over the entire band are, respectively, reasonably flat and uniform. This demonstrates that the eight-way power divider used in the feeding network distributes the signals with uniform power and uniform phase very well.

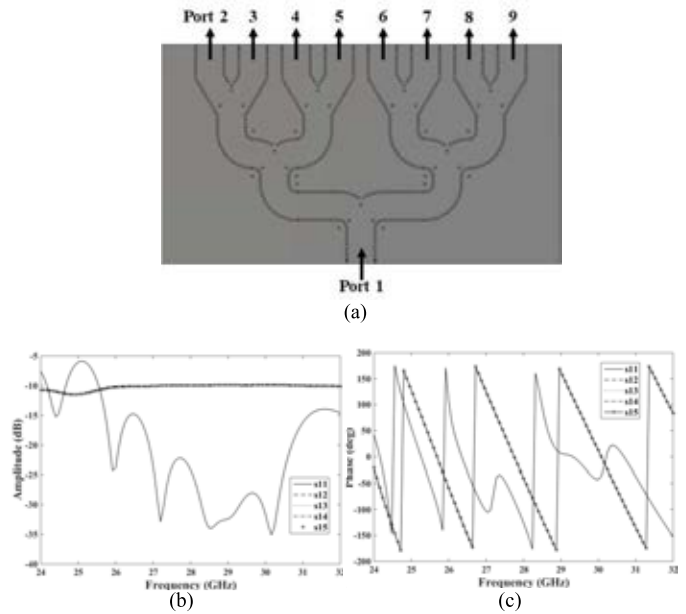


Fig. 7. Geometry and simulated S-parameters of the eight-way power divider used in the feeding network. (a) Geometry. (b) Amplitude. (c) Phase.

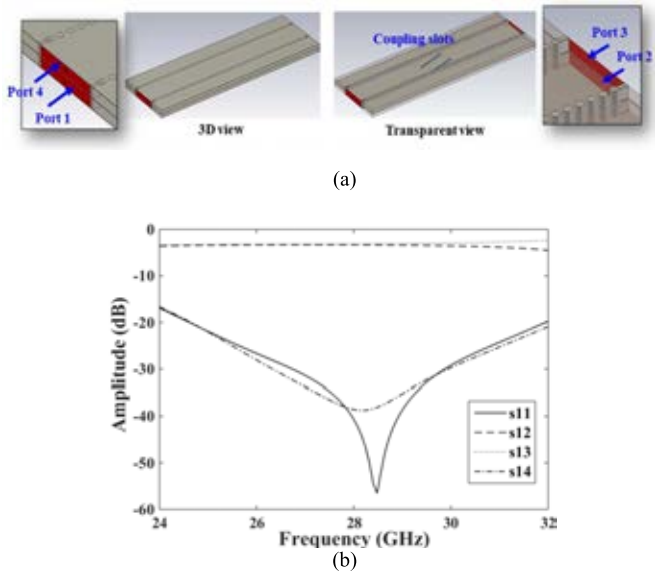


Fig. 8. Geometry and simulated S-parameter of double-layer SIW directional coupler. (a) Geometry. (b) S-parameter.

The simulation was conducted to verify the performance of the multilayer directional coupler to combine the calibration signal with the received signal. Fig. 8 illustrates the geometry of the double-layer SIW directional coupler and the simulation result. There are two coupling slots etched on the central metal plane to divide the input signal from port 1 into ports 2 and 3. The reflection coefficient ($|S_{11}|$) and isolation ($|S_{41}|$) characteristics of the coupler are less than -30 dB over the operating frequency band. The insertion losses ($|S_{21}|$ and $|S_{31}|$) of the coupler are less than 3.3 dB across the operating frequency band. It is confirmed by the result of S-parameter

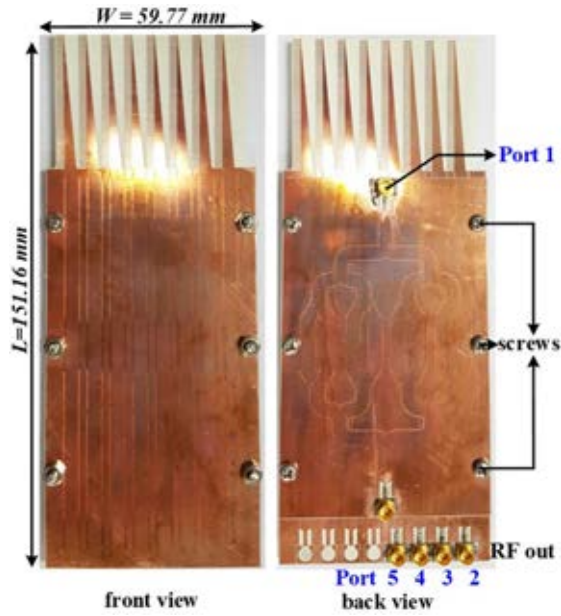


Fig. 9. Photograph of the fabricated TSA array with calibration coupler for calibration signal input.

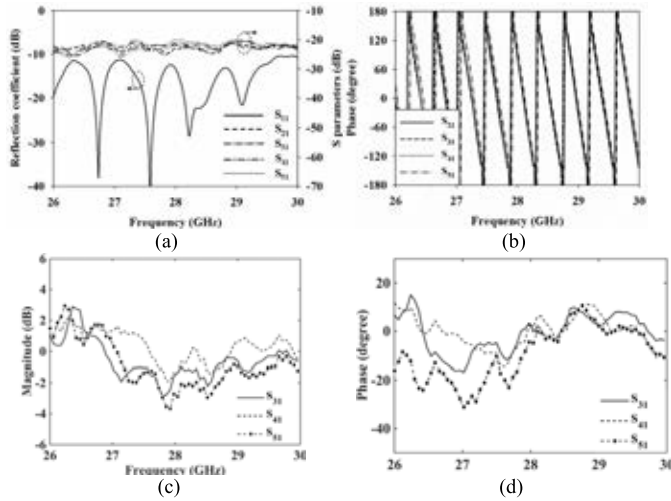


Fig. 10. Measured S-parameters of the calibration signal path of the proposed TSA array. (a) Magnitude of S-parameter. (b) Phase of S-parameter. (c) Relative error of magnitude. (d) Relative error of phase.

that the calibration signal is well combined with the received signal through the coupler.

C. Performance of Calibration Signal Path

The two layers of TSA array were stacked up and fixed with screws as shown in Fig. 9. The calibration signal is propagated from port 1 and divided through the eight-way power divider. The divided calibration signals with the same phase and amplitude are transferred to the RF lines. To verify the performance of the calibration signal path, S-parameters of it were measured at each RF output. The measured S-parameters of the calibration signal path of the proposed 1×8 array TSA are shown in Fig. 10. The reflection coefficient of calibration port 1 is less than -10 dB over the entire frequency band. The

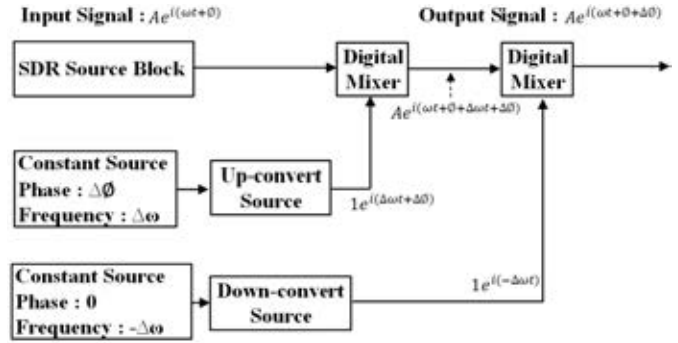


Fig. 11. Block diagram of a digital phase shifter.

magnitude of the each output of the calibration signal path is about -22 dB and the relative magnitude errors of each path compared to S_{21} are within 4 dB over the operating frequency band. The relative phase errors of each path are within 30° over the operating frequency band. Since the design was made considering the main frequency (28 GHz), it can be confirmed that the relative error becomes larger as the distance from the center frequency increases. However, the fabrication errors are considered and removed as a part of offset elimination in the calibration process.

IV. SIGNAL PROCESSING PART

A. New Type of Digital Phase Shifter

In a fully digital beamforming architecture, the phase shifter can be implemented digitally. In the proposed FDBR, a new type of digital phase shifter is applied and the digital phase shifter is able to accurately adjust the phase without offset error and variation error according to the temperature. In addition, since the digital phase shifter has extremely high control resolution, high-performance beamforming is possible with low sidelobe level and no gain reduction due to the offset error and variation error [32].

The proposed digital phase shifter consists of two digital mixers and two signal sources as shown in Fig. 11. The two signal sources, coded using C++ in GNUradio, digitally produce a signal with the desired phase. In Fig. 11, the upconvert source generates a signal with the magnitude 1 and the phase $\Delta\phi$, and upfrequency $\Delta\omega$. The downconvert signal source generates a signal with the magnitude 1, the phase 0, and the downfrequency $-\Delta\omega$ to cancel the up-frequency. The input signal is converted into output signal by mixing the input signals with the two signal sources in the two mixer. The output signal is only shifted by a phase of $\Delta\phi$, compared with input signal, without changing amplitude. Fig. 12 presents the simulation result of phase control. The simulation result demonstrates that the desired phase is accurately shifted without error.

The resolution of the digital phase shifter is equal to the phase control resolution of the upconvert signal because the phase of the upconvert signal is added to the input signal through the mixer. Since the upconvert signal is a digitized signal, the interval between samples is the phase control

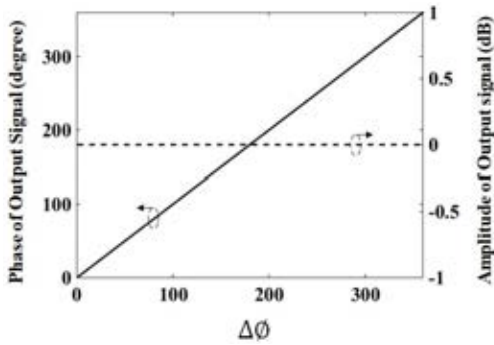


Fig. 12. Simulation result of digital phase shifter.

resolution. Therefore, the adjustable minimum phase is

$$Ph_m = \frac{360}{N_{\lambda_0}} \quad (1)$$

where Ph_m is the adjustable minimum phase and N_{λ_0} is the number of samples in a wavelength of the upconvert signal source.

In other words, as the number of samples in a wavelength of the upconvert signal increases, the digital phase shifter has a higher resolution. The number of samples in a wavelength of the upconvert signal is associated with the sampling rate and upconvert frequency. In GNUradio, the upconvert source generates a signal in synchronization with the sampling rate. Thus, the number of samples in a wavelength (N_{λ_0}) is

$$N_{\lambda_0} = \frac{f_s}{f_{up}} \quad (2)$$

where f_s is the sampling rate and f_{up} is the upconvert frequency.

As the upconvert frequency decreases, the number of samples in a wavelength increases. Therefore, since the upconvert frequency can be adjusted down to 1 Hz, the adjustable minimum phase is theoretically 0.000018° based on the maximum specification of the SDR. However, if the maximum specifications of the SDR are applied to the FDBR with eight chains, there is a distortion in data transmission. Thus, optimization of the values such as sampling rate and digital upconvert/downconvert frequency is necessary. The optimized sampling rate is 10 MHz and the digital upconvert /downconvert frequency is 20 kHz. Finally, the adjustable minimum phase is 0.72° in the FDBR. If an SDR and PC with better specification are used, the higher resolution that meets the theoretical value can be obtained. It is impossible to have the resolution of 0.72° for the conventional phase shifter based on a chip, and only possible in the digital phase shifter that manipulates digitized signals. The digital phase shifter with extremely high performance is applied to the FDBR with the calibration approach.

B. Beamforming With Real-Time Calibration Blocks

In the signal processing parts, the received signals are calibrated and used for beamforming in real time. A two chain calibration architecture is presented in Fig. 13. The

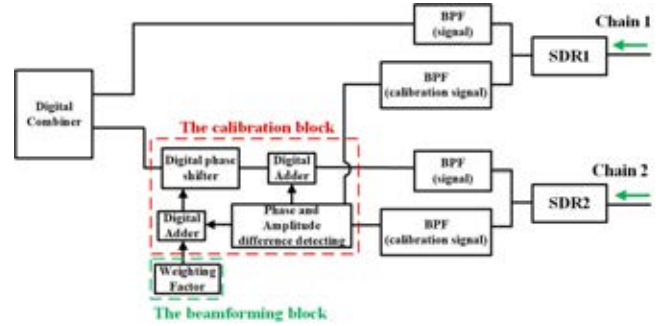


Fig. 13. Block diagram of real-time calibration with digital phase shifter.

architecture of the signal processing parts consists of the phase and amplitude difference detecting block, the digital BPF, the digital adder, the digital amplifier, the digital phase shifter, and the weighting factor block. The signals received from chains 1 and 2 are, respectively, separated into the received signal and the calibration signal through the digital BPF which can separate signals very accurately. The separated calibration signals of chain 1 and chain 2 then move to the difference detecting block, where the phase and amplitude difference between chain 1 and chain 2 signals are measured. The measured amplitude difference is transferred to the digital amplifier to correct the amplitude difference of the received signals in chain 2. The measured phase difference is added to the weighting factor via the digital adder, and then pass to the digital phase shifter. Then, the phase of the received signal in chain 2 is shifted by the phase difference and the weighting factor. The final output signal of chain 2 is calibrated based on chain 1, and additionally the output phase is shifted by the weighting factor. By applying this architecture to all chains, the signals of all chains can be calibrated based on chain 1 in real time, and at the same time, beamforming with accurate performance is possible.

V. PERFORMANCE OF THE REAL-TIME CALIBRATION METHOD AND BEAMFORMING

A. Real-Time Calibration Method

To verify the performance of the real-time calibration, we measured the phase and amplitude errors of all chains after the calibration with respect to chain 1 for 4 h. The measurement was carried out at intervals of 2 min in the first 1 h when there are relatively large changes, and then, the measurement was performed at intervals of 20 min for the remaining time. The measured average errors of the eight chains after the calibration are listed in Table IV.

After the calibration, the amplitude error and phase error among chains are quite low, as shown in Fig. 14. Among all chains, the average amplitude error is less than 0.5 dB and the average phase error is less than 0.9° after the calibration. It can be confirmed that the errors generated due to the active component of the FDBR are precisely removed.

TABLE IV
MEASURED ERRORS (UNIT: DECIBEL AND DEGREE)

		After Calibration							
		Chain							
		1	2	3	4	5	6	7	8
Amplitude	Average Error	0	0.5	0.1	0.3	0.1	0.2	0.3	0.4
phase	Average Error	0	0.8	0.2	0.9	0.7	0.4	0.7	0.5

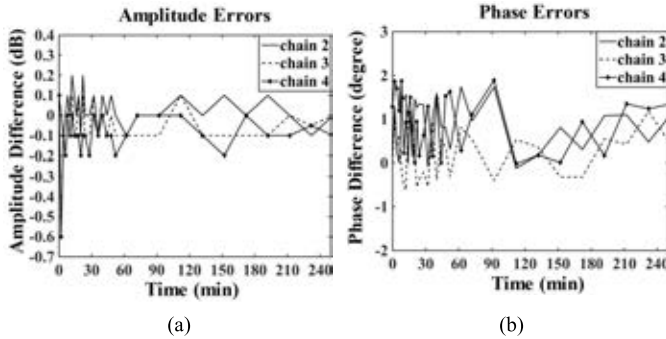


Fig. 14. Measured errors in the FDBR for 4 h after calibration. (a) Amplitude. (b) Phase.

TABLE V
WEIGHTING FACTOR (UNITS: DEGREE)

Beam Angle	Weighting Factor							
	\varnothing_1	\varnothing_2	\varnothing_3	\varnothing_4	\varnothing_5	\varnothing_6	\varnothing_7	\varnothing_8
0	0	0	0	0	0	0	0	0
15	-193.9	-138.5	-83.1	-27.7	27.7	83.1	138.5	193.9
30	-374.6	-267.6	-160.5	-53.5	53.5	160.5	267.6	374.6
45	-529.8	-378.4	-227.0	-75.6	75.6	227.0	378.4	529.8

B. Beamforming Performance of the Proposed FDBR

The measurements of radiation pattern are conducted to demonstrate the performance of beamforming with the calibration in far-field AC. A 1×4 patch antenna array similar to [33] is used as a transmitter antenna and a signal generator (Agilent E8257D) is used as signal source for exact measurement. In order to synchronize the transmitter and the proposed FDBR, a 10 MHz clock signal of the FDBR is used as external clock signal of the signal generator. The weighting factor for 0° , 15° , 30° , and 45° scan angles is calculated and listed in Table V.

The frequency of the signal is 28 GHz and the frequency of the calibration signal is 28.002 GHz. Thus, they are 2 MHz apart. Fig. 15 shows the simulated normalized radiation patterns of the proposed 1×8 array TSA and the measured normalized radiation patterns using the fabricated FDBR for 0° , $\pm 15^\circ$, $\pm 30^\circ$, and $\pm 45^\circ$ at 28 GHz. The measured radiation patterns are well matched with the simulated radiation patterns. The error of the main beam directions is within 1° , and the error in the gain of the main lobe is within 0.5 dB, which is an accurate beamforming performance.

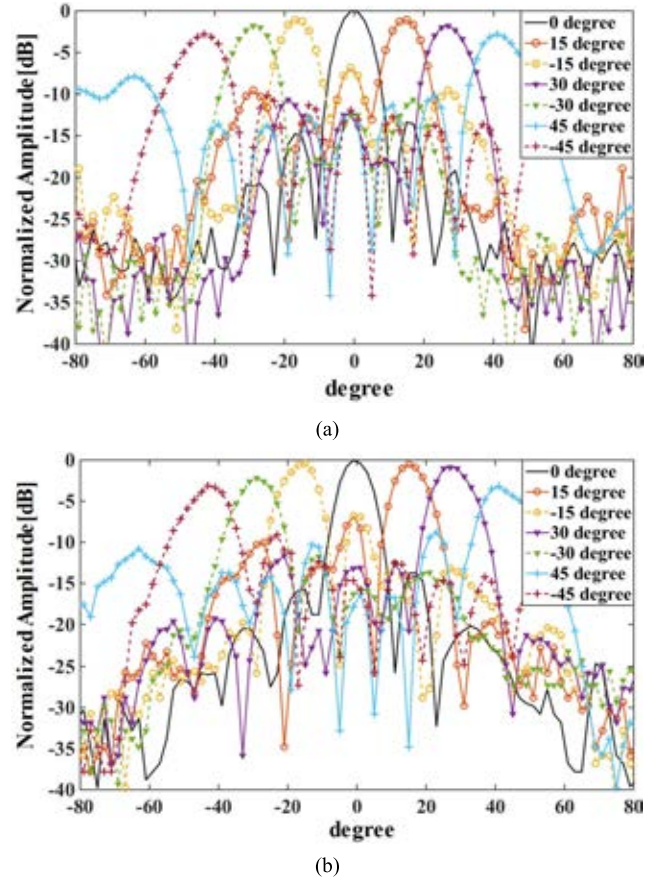


Fig. 15. (a) Simulated beamforming result of the proposed 1×8 array TSA. (b) Measured beamforming result of the proposed 1×8 array TSA using the FDBR.

VI. CONCLUSION

Currently, beamforming technology is regarded as the solution for 5G communication, but beamforming system developers have difficulties in its implementation. In this paper, a real-time calibration is applied to calibrate the errors generated in active component, and the difficulties in applying the real-time calibration at mm-wave band are solved by combining the directional coupler, SIW structure, and uniform divider with TSA antenna. Finally, this paper presents the FDBR, which has a new structure that can simultaneously perform beamforming and real-time calibration targeting user equipment (UE) of 5G mobile communication at mm-wave band, for the first time. The proposed FDBR has a very simple structure and the calibration method significantly reduces the phase and amplitude errors. The average amplitude errors in all chains are less than 0.5 dB and the average phase errors in all chains are less than 0.9° after the calibration. The simulated radiation pattern results and measured radiation pattern results of the proposed FDBR are compared, and found to be well matched. Very low error of main beam direction and gain has been demonstrated. The error of main beam direction is less than 1° and the error of gain is less than 0.5 dB. The proposed FDBR with the calibration method is suitable for accurate beamforming at 28 GHz band. This makes it an attractive candidate for 5G communication.

REFERENCES

- [1] Y. Li, J. Wang, and K.-M. Luk, "Millimeter-wave multibeam aperture-coupled magnetoelectric dipole array with planar substrate integrated beamforming network for 5G applications," *IEEE Trans. Antennas Propag.*, vol. 65, no. 12, pp. 6422–6431, Dec. 2017.
- [2] J. Lota, S. Sun, T. S. Rappaport, and A. Demosthenous, "5G uniform linear arrays with beamforming and spatial multiplexing at 28, 37, 64, and 71 GHz for outdoor urban communication: A two-level approach," *IEEE Trans. Veh. Technol.*, vol. 66, no. 11, pp. 9972–9985, Nov. 2017.
- [3] O. Jo, J.-J. Kim, J. Yoon, D. Choi, and W. Hong, "Exploitation of dual-polarization diversity for 5G millimeter-wave MIMO beamforming systems," *IEEE Trans. Antennas Propag.*, vol. 65, no. 12, pp. 6646–6655, Dec. 2017.
- [4] S. Han, C.-L. I, Z. Xu, and C. Rowell, "Large-scale antenna systems with hybrid analog and digital beamforming for millimeter wave 5G," *IEEE Commun. Mag.*, vol. 53, no. 1, pp. 186–194, Jan. 2015.
- [5] J. S. Herd and M. D. Conway, "The evolution to modern phased array architectures," *Proc. IEEE*, vol. 104, no. 3, pp. 519–529, Mar. 2016.
- [6] B. Sadhu *et al.*, "A 28-GHz 32-element TRX phased-array IC with concurrent dual-polarized operation and orthogonal phase and gain control for 5G communications," *IEEE J. Solid-State Circuits*, vol. 52, no. 12, pp. 3373–3391, Dec. 2017.
- [7] D.-W. Kang, J.-G. Kim, B.-W. Min, and G. M. Rebeiz, "Single and four-element *Ka*-band transmit/receive phased-array silicon RFICs with 5-bit amplitude and phase control," *IEEE Trans. Microw. Theory Techn.*, vol. 57, no. 12, pp. 3534–3543, Dec. 2009.
- [8] A. Natarajan *et al.*, "A fully-integrated 16-element phased-array receiver in SiGe BiCMOS for 60-GHz communications," *IEEE J. Solid-State Circuits*, vol. 46, no. 5, pp. 1059–1075, May 2011.
- [9] W.-L. Chen, S.-F. Chang, K.-M. Chen, G.-W. Huang, and J.-C. Chang, "Temperature effect on *Ku*-band current-reused common-gate LNA in 0.13- μm CMOS technology," *IEEE Trans. Microw. Theory Techn.*, vol. 57, no. 9, pp. 2131–2138, Sep. 2009.
- [10] L. Xie, X. Yin, C. Lu, L. Yang, H. Zhao, and S. Li, "Hybrid analog-digital antenna array with built-in image injection calibration," *IEEE Trans. Antennas Propag.*, vol. 62, no. 11, pp. 5513–5523, Nov. 2014.
- [11] L. Wu, H. F. Leung, and A. Li, "A 4-element 60-GHz CMOS phased-array receiver with beamforming calibration," *IEEE Trans. Circuits Syst. I, Reg. Papers*, vol. 64, no. 3, pp. 642–652, Mar. 2017.
- [12] D. Bekers, R. van Dijk, and F. van Vliet, "Mutual-coupling based phased-array calibration: A robust and versatile approach," in *Proc. IEEE Int. Symp. Phased Array Syst. Technol.*, Oct. 2013, pp. 630–637.
- [13] C. Shipley and D. Woods, "Mutual coupling-based calibration of phased array antennas," in *Proc. IEEE Int. Symp. Phased Array Syst. Technol.*, May 2000, pp. 529–532.
- [14] B. Brütigam, J. H. González, M. Schwerdt, and M. Bachmann, "TerraSAR-X instrument calibration results and extension for TanDEM-X," *IEEE Trans. Geosci. Remote Sens.*, vol. 48, no. 2, pp. 702–715, Feb. 2010.
- [15] M. K. Hedayati, A. Abdipour, R. S. Shirazi, C. Cetintepe, and R. B. Staszewski, "A 33-GHz LNA for 5G wireless systems in 28-nm bulk CMOS," *IEEE Trans. Circuits Syst. II, Exp. Briefs*, vol. 60, no. 10, pp. 1460–1464, Oct. 2018.
- [16] W. Hong, K.-H. Baek, and S. Ko, "Millimeter-wave 5G antennas for smartphones: Overview and experimental demonstration," *IEEE Trans. Antennas Propag.*, vol. 65, no. 10, pp. 6250–6261, Dec. 2017.
- [17] J. Bang and J. Choi, "A SAR reduced mm-wave beam-steerable array antenna with dual-mode operation for fully metal-covered 5G cellular handsets," *IEEE Antennas Wireless Propag. Lett.*, vol. 17, no. 6, pp. 1118–1122, Jun. 2018.
- [18] O. Bakr and M. Johnson, "Impact of phase and amplitude errors on array performance," Dept. EECS, Univ. California, Berkeley, Berkeley, CA, USA, Tech. Rep. UCB/EECS-2009-1, 2009.
- [19] M. Willerton, D. Yates, V. Goverdovsky, and C. Papavassiliou, "Experimental characterization of a large aperture array localization technique using an SDR testbench," in *Proc. Wireless Innov. Forum Conf. Commun. Technol. Softw. Defined Radio*, vol. 2. Washington, DC, USA, Nov./Dec. 2011, pp. 1–7.
- [20] H. Q. Nguyen, J. S. Whittington, J. C. Devlin, H. L. Vu, N.-V. Vu, and E. Custovi, "Accurate phase calibration for digital beam-forming in multi-transceiver HF radar system," *Int. J. Electron. Telecommun.*, vol. 59, no. 3, pp. 245–254 2013.
- [21] S. Zeinolobedinzadeh, A. Ç. Ulusoy, M. A. Oakley, N. E. Lourenco, and J. D. Cressler, "A 0.3–15 GHz SiGe LNA with >1 THz gain-bandwidth product," *IEEE Microw. Wireless Compon. Lett.*, vol. 27, no. 4, pp. 380–382, Apr. 2017.
- [22] U. Mayer, F. Ellinger, and R. Eickhoff, "Analysis and reduction of phase variations of variable gain amplifiers verified by CMOS implementation at C-band," *IET Circuits, Devices Syst.*, vol. 4, no. 5, pp. 433–439, Sep. 2010.
- [23] K.-Y. Kao, D.-R. Lu, J.-C. Kao, and K.-Y. Lin, "A 60 GHz variable-gain low-noise amplifier with low phase variation," in *Proc. IEEE Int. Symp. Radio-Freq. Integr. Technol. (RFIT)*, Taipei, Taiwan, Aug. 2016, pp. 1–3.
- [24] D.-S. Siao, J.-C. Kao, and H. Wang, "A 60 GHz low phase variation variable gain amplifier in 65 nm CMOS," *IEEE Microw. Wireless Compon. Lett.*, vol. 24, no. 7, pp. 457–459, Jul. 2014.
- [25] NR; *User Equipment (UE) Radio Transmission and Reception; Part 2: Range 2 Standalone (Release 15)*, document TS 38.101-2, 2018.
- [26] B. Yang, Z. Yu, Y. Dong, J. Zhou, and W. Hong, "Compact tapered slot antenna array for 5G millimeter-wave massive MIMO systems," *IEEE Trans. Antennas Propag.*, vol. 65, no. 12, pp. 6721–6727, Dec. 2017.
- [27] S.-J. Park, D.-H. Shin, and S.-O. Park, "Low side-lobe substrate-integrated-waveguide antenna array using broadband unequal feeding network for millimeter-wave handset device," *IEEE Trans. Antennas Propag.*, vol. 64, no. 3, pp. 923–932, Mar. 2016.
- [28] O. Kramer, T. Djerafi, and K. Wu, "Dual-layered substrate-integrated waveguide six-port with wideband double-stub phase shifter," *IET Microw., Antennas Propag.*, vol. 6, no. 15, pp. 1704–1709, Dec. 2012.
- [29] M. I. Nawaz, Z. Huiling, and M. Kashif, "Substrate integrated waveguide (SIW) to microstrip transition at X-Band," in *Proc. Int. Conf. Circuits, Syst. Control*, 2014, pp. 61–63.
- [30] L. Yan, W. Hong, K. Wu, and T. J. Cui, "Investigations on the propagation characteristics of the substrate integrated waveguide based on the method of lines," *IEE Proc.-Microwaves, Antennas Propag.*, vol. 152, no. 1, pp. 35–42, Feb. 2005.
- [31] T. Djerafi and K. Wu, "Corrugated substrate integrated waveguide (SIW) antipodal linearly tapered slot antenna array fed by quasi-triangular power divider," *Prog. Electromagn. Res. C*, vol. 26, pp. 139–151, Dec. 2012.
- [32] H. Kamoda, J. Tsumochi, and F. Suginoshi, "Reduction in quantization lobes due to digital phase shifters for phased array radars," in *Proc. Asia-Pacific Microw. Conf. (APMC)*, 2011, pp. 1618–1621.
- [33] S.-J. Park and S.-O. Park, "LHCP and RHCP substrate integrated waveguide antenna arrays for millimeter-wave applications," *IEEE Antennas Wireless Propag. Lett.*, vol. 16, pp. 601–604, 2017.



Dong-Chan Kim received the B.S. degree in electronic and electrical engineering from Sungkyunkwan University, Suwon, South Korea, in 2015, and the M.S. degree from the School of Electrical Engineering, Korea Advanced Institute of Science and Technology, Daejeon, South Korea, in 2017, where he is currently pursuing the Ph.D. degree.

His current research interests include the design of frequency-modulated continuous wave radar systems, radar signal processing, and digital beamforming.



Seong-Jin Park received the B.S. degree in electronic engineering from Korea Aerospace University, Goyang, South Korea, in 2014, and the integrated M.S. and Ph.D. degrees from the School of Electrical Engineering, Korea Advanced Institute of Science and Technology, Daejeon, South Korea, in 2018.

Since 2018, he has been with Samsung Electronics, Suwon, South Korea. His current research interests include the design of millimeter-wave antenna, radar systems, and channel measurement.



Tae-Wan Kim received the B.S. degree in electronic and electrical engineering from the University of Konkuk, Seoul, South Korea, in 2013, and the M.S. degree from the School of Electrical Engineering, Korea Advanced Institute of Science and Technology, Daejeon, South Korea, in 2015, where he is currently pursuing the Ph.D. degree.

His current research interests include ferrite-loaded antennas and material measurement.



Laxmikant Minz was born in Katihar, India, in 1986. He received the B.Tech. degree in electronic and communication engineering from NIT Nagpur, Nagpur, India, in 2007, and the M.Tech. degree in RF and microwave engineering from IIT Kharagpur, Kharagpur, India, in 2009. He is currently pursuing the Ph.D. degree with the School of Electrical Engineering, Korea Advanced Institute of Science and Technology, Daejeon, South Korea.

He was a Researcher with Antenna Development Team, ETRI, Daejeon. His current research interests include antenna and array design, microstrip miniaturized antenna, radar system, metamaterial, electromagnetics, and microwave circuit design.



Seong-Ook Park (M'05–SM'11) received the B.S. degree in electrical engineering from KyungPook National University, Daegu, South Korea, in 1987, the M.S. degree in electrical engineering from the Korea Advanced Institute of Science and Technology, Daejeon, South Korea, in 1989, and the Ph.D. degree in electrical engineering from Arizona State University, Tempe, AZ, USA, in 1997.

From 1989 to 1993, he was a Research Engineer with Korea Telecom, Daejeon, where he was involved in microwave systems and networks. He joined the Telecommunication Research Center, Arizona State University, until 1997. Since 1997, he has been a Professor with the Korea Advanced Institute of Science and Technology. His current research interests include antenna, radar system, and analytical and numerical techniques in the area of electromagnetics.